Journal of Materials Chemistry A

ROYAL SOCIETY OF CHEMISTRY

PAPER

Cite this: DOI: 10.1039/d5ta08440g

Thermal treatment of high-density polyethylene films to increase crystallinity for the fabrication of superior radiation-grafted anion-exchange membranes for fuel cells

Siân A. Franklin, [a] Mozhdeh Mohammadpour, [c] Yingdan Cui, [b] Rachida Bance-Soualhi, [a] Carol Crean, [a] William E. Mustain, [b] Hungyen Lin [cd] and John R. Varcoe *[a]

When fabricating radiation-grafted anion exchange membrane (RG-AEMs), it is important to understand the microstructure of the precursor film (such as high-density polyethylene, HDPE). This study builds on recent work showing that variations in the degree of crystallinity of the HDPE precursor led to variations in the final RG-AEM properties (up to a threshold of 81%, above which the properties become more consistent). This study shows that the degree of crystallinity of the HDPE film can be increased to >81% by thermal treatment at 115 °C for 24 h (followed by natural cooling in the oven). In addition to increasing the bulk degree of crystallinity, it was shown that thermal treatment increased crystalline domain sizes and lamella width distributions, while it reduced orientational order of the lamellae. The treated HDPE films resulted in optimised RG-AEMs with increased IECs and water uptakes values at high relative humidities (RH > 70%); there was also a small improvement in Cl^- conductivities in water. Terahertz time domain spectroscopy (THz-TDS) showed that the proportion of bulk water present in the optimised RG-AEM was greater than its untreated counterpart (66% *vs.* 58% when fully hydrated); bulk water is essential for high ion conductivities and rapid water diffusion. In fuel cell testing, the optimised RG-AEM had improved *in situ* water transport compared to the untreated benchmark, as it required lower operating RHs to achieve a peak power density of 2.8 W cm^{-2}. Furthermore, the optimised RG-AEM maintained a higher operating current at intermediate voltages, 2.7 A cm^{-2} at 0.7 V *vs.* 2.1 A cm^{-2} for the benchmark RG-AEM.

Received 16th October 2025
Accepted 22nd December 2025

DOI: 10.1039/d5ta08440g

rsc.li/materials-a

Background and context

Anion exchange membranes (AEMs) typically consist of cationic groups that are covalently attached to a polymer backbone; common cationic groups include quaternary ammoniums and imidazolium chemistries.[1–3] Use of an AEM allows for the preferential conduction of target anions, whilst maintaining an impermeable barrier for electrons and reactants (*e.g.* H_2 and O_2 gases). AEMs are located at the core of electrochemical devices such as fuel cells (AEMFC). AEMs deployed in such technologies must exhibit high ionic conductivities, facile water transport behaviours, and high chemical and mechanical durabilities.[4,5]

Many effective AEMs consist of a hydrophilic phase, which controls ion and H_2O transport, and a hydrophobic phase, which influences mechanical and barrier properties. The physical properties of an AEM, including conductivity and dimensional stability, are strongly dependent on the AEM's morphology, both at the micro and nano phase.[6–10] For example, Lee *et al.* compared the use of *meta*- and *para*-terphenyl repeat units in AEM backbones to demonstrate the impact that such geometry had on both the microstructure and the resultant AEM properties.[11] The use of the more flexible *meta*-monomer allowed increased interaction between the hydrocarbon backbone chain resulting in more obvious phase separation; this led to an improved ion conductivity at 80 °C of 122 mS cm^{-1} (*vs.* 81 mS cm^{-1} with the *para*-monomer under the same conditions).[11]

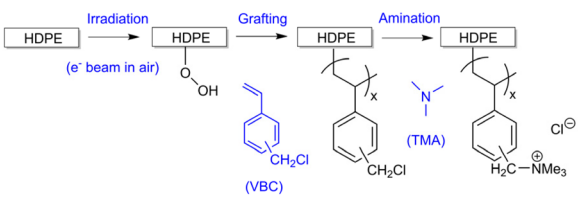

Scheme 1 An outline of the synthesis of the HDPE-based radiation grafted anion-exchange membranes (RG-AEM).

[a]School of Chemistry and Chemical Engineering, The University of Surrey, Guildford GU2 7XH, UK. E-mail: j.varcoe@surrey.ac.uk
[b]Department of Chemical Engineering, Swearingen Engineering Center, University of South Carolina, 301 Main St., Columbia, SC 29208, USA
[c]School of Engineering, Lancaster University, Lancaster, LA1 4YW, UK
[d]School of Engineering, University of Warwick, Coventry CV4 7AL, UK

Sproll *et al.* used small angle X-ray scattering to compare the crystallite size of ethylene-*alt*-tetrafluoroethylene (ETFE) polymer film, from two different commercial suppliers.[12] These films were then used to fabricate radiation-grafted proton exchange membranes (RG-PEMs). The difference in arrangement of the crystalline phase (in otherwise identical films) was shown to influence the macroscopic properties of the PEM. The RG-PEM made from ETFE from Dupont had a larger crystallite size (13.1 ± 0.2 nm) compared to that made from ETFE supplied by Saint-Gobain (10.6 ± 0.1 nm) and demonstrated higher PEM fuel cell performance and greater stability during humidity cycling (showing only 19% performance loss with respect to initial performance compared to a 35% loss with the Saint-Gobain based RG-PEM, when performance was measured at 50% relative humidity, RH).[12]

Our study focuses on the development of radiation-grafted (RG) AEMs (Scheme 1) where a commercial high-density polyethylene (HDPE) film is irradiated at high energy, using an electron-beam, and subsequently grafted and aminated. In the past, to control the degree of grafting (DoG) and the microstructure of the final RG-AEMs, investigations have focused on controlling the grafting monomer, quaternary head group chemistry, and/or the grafting reaction conditions.[13–16] For example, Zhao *et al.* investigated the effect of the DoG on the resultant RG-AEM morphology.[6] Using partial X-ray scattering function analysis, it was demonstrated that above a critical DoG value, there was a morphological inversion between the hydrophobic and hydrophilic phases (a fundamental change in the RG-AEM microstructure), leading to an increase in water uptake (WU) and conductivity.

There has been limited work however, on understanding how the precursor film morphology (crystallinity prior to e^--beam irradiation) influences RG-AEM properties.[17] In our previous work,[18] we have shown that unavoidable variations in the manufacturing process results in measurable differences in crystallinity along and between commercial rolls of 10 μm thick HDPE film. The variation in the precursor film crystallinity was shown to impact DoG and RG-AEM properties including ion exchange capacity (IEC), conductivity and WU. With this specific HDPE substrate, we clearly showed that above degree of crystallinity values of *ca.* 81%, changes in crystallinity did not lead to significant changes in RG-AEM properties, whereas below this threshold, changes in crystallinity led to more variable RG-AEM properties.[18] If RG-AEMs are to be manufactured on a larger scale, it is imperative that the RG-AEMs produced are reproducible and consistent, so we targeted a HDPE substrate crystallinity of >81%. With such a scale-up in mind, the aim of this study was to:

(1) Develop a thermal method to reduce crystallinity variation across a commercially supplied HDPE film whilst controlling the degrees of crystallinity to be >81%.

(2) Understand how the thermal treatment impacts the microstructure of the HDPE precursor film.

(3) Compare RG-AEM properties and performances between those made with a thermally treated HDPE film *vs.* a benchmark untreated precursor HDPE film.

Experimental

Materials and chemicals

HDPE film with a thickness of 10 μm, a width of 600 mm and a length of 30 m was purchased from Goodfellow (UK) in September 2023 (ET32-FM-000110, batch number 301004798). For RG-AEM synthesis, vinybenzyl chloride (VBC) monomer (*m*- and *p*-isomer mixture, stabilised with 4-*tert*-butylcatechol inhibitor, ONP and *o*-nitrocresol) was purchased from TCI Europe; the inhibitor was removed before use by passing the monomer through a column of aluminium oxide, purchased from Merck. Toluene (≥99.5% purity), 1-octyl-2-pyrrolidone (98% purity), aqueous trimethylamine solution (TMA, 45% mass), and NaCl (>99% purity), were purchased from Merck and used as received. Deionised (DI, grade II) water was used during the grafting and washing stages of the synthesis, whilst ultrapure water (UPW) with a resistivity of 18.2 MΩ cm was used in the final ion-exchange and analytical experiments. To complete titrations, sodium nitrate ($NaNO_3$, extra pure) and silver nitrate ($AgNO_3$, 0.02 M) were purchased from Thermo Fisher Scientific and aqueous nitric acid (HNO_3, 1 M) was bought from Merck.

To prepare the gas diffusion electrodes (GDEs) for AEMFC testing, 60% mass PtRu on Vulcan XC-72 carbon (PtRu/C, 1 : 1 atomic ratio, SKU: 592678-1, Fuel Cell Store), 40% mass Pt on carbon black (Pt/C, SKU: 47308, Alfa Aesar), and Vulcan XC-72R carbon (Product Code: VXC72R, Cabot) were used as catalysts. An ETFE-based benzyltrimethylammonium-type radiation-grafted polymer powder (IEC $= 2.1 \pm 0.2$ mmol g^{-1}) was synthesised in-house following our previously reported method and was employed as the anion exchange ionomer.[19,20] Hydrophobic polytetrafluoroethylene (PTFE) powder (Ultraflon MP-25, Product Code: 48080001, Fuel Cell Store) was incorporated into the catalyst layers (CLs) to enhance water management. Toray 060 Carbon Paper with 5% mass wet proofing (SKU: 591037, Fuel Cell Store) was used as the gas diffusion layer (GDL) for both the anode and cathode electrodes. Isopropanol (IPA, Thermo Fisher Scientific) and Millipore deionised UPW were used as solvents. Ultra-high purity N_2, O_2 and H_2 gases were supplied by Airgas and used for all fuel cell experiments.

Heat treatment procedures

HDPE film was cut to size and placed in a Memmert universal oven pre-set to 20 °C. The oven was then set to the chosen temperature (50, 85 or 115 °C) with a heating rate of 1 °C min^{-1}. The film was held for the desired time (2 or 24 h) before being allowed to cool naturally (waiting until the samples returned to room temperature after turning off the oven, the cooling rate averaged 0.65 °C min^{-1}).

Differential scanning calorimetry (DSC)

Samples (10–15 mg) were cut and layered into a Tzero aluminium pan. A DCS250 (TA Instruments) was then used to complete a heat cool cycle between 25 °C and 200 °C with a 2 min isothermal hold at 200 °C. The heating and cooling rate was set to 10 °C min^{-1}. The degree of crystallinity (x_c) was calculated using eqn (1), where ΔH_m is the measured enthalpy of melting (J g^{-1}) calculated by integrating the area of the endothermic melting

peak using Trios software, and ΔH_{total} is the total enthalpy of a 100% crystalline sample, taken as 293 J g^{-1}.[21,22]

$$x_c\ (\%) = 100 \times (\Delta H_m/\Delta H_{total}) \quad (1)$$

Density measurements

Samples (15 × 10 cm) were pressed into $\frac{1}{4}$ inch pellets using a Specac manual hydraulic press (3 tonnes for 4 min). The pellet was subsequently placed in a 5 cm^3 sample holder and the density was measured using an Accupyc II 1345 pycnometer operating with Helium. For each sample, 10 repeat measurements were taken and the mean was calculated. x_c was calculated using eqn (2), where ρ_a is the theoretical density of a 100% amorphous polyethylene (PE) sample (0.85 g cm^{-3}), ρ_c is the theoretical density of a 100% crystalline PE sample (1.00 g cm^{-3}), and ρ is the density of the measured sample.[23,24]

$$x_c\ (\%) = 100 \times \rho_c(\rho - \rho_a)/\rho(\rho_c - \rho_a) \quad (2)$$

Raman spectroscopy

An InVia Reflex Raman Microscope (Renishaw, UK) fitted with a cooled charged couple detector, holographic notch filters, a 2400 mm^{-1} grating, and a 457 nm excitation laser was used to record all spectra. A Leica DMLM optical microscope and a trinocular viewer to allow direct viewing of the sample was also attached.[25] Raw data was processed using WiRE 4.2 software (including peak fitting).

For mapping of the HDPE films, a 100× magnification near working distance objective (aperture number NA = 0.85) was used. The map was obtained using 1 μm steps across a 20 μm × 20 μm area. A single accumulation, *ca.* 19 mW power at sample, and an exposure time of 0.2 s was used to acquire each spectrum. Processing involved truncation (to 1000–1600 cm^{-1}), baseline correction (using intelligent fitting with anchored end points, polynomial order 11, noise tolerance 1.5), cosmic ray removal and smoothing (polynomial order 2, smooth window size 7). x_c was determined using the calculated amorphous content (α_a) as shown in eqn (3) and (4).[21] A_{1305} refers to the integrated area of the 1305 cm^{-1} band which was fitted using an optimised contribution of the Gaussian/Lorentz functions; the fitting range was set between 1220 and 1550 cm^{-1}, the band was fixed between 1303 and 1309 cm^{-1} and, the number of fitting iterations was capped at 200. The reference peak, A_{ref}, was calculated by directly integrating between 1253–1352 cm^{-1}.

$$x_c\ (\%) = 100 \times (1 - \alpha_a) \quad (3)$$

$$\alpha_a = A_{1305}/A_{ref} \quad (4)$$

To measure spectra of the grafted and aminated membranes for functional group characterisation, a 20× (NA = 0.40) objective was used. Spectra were recorded with *ca.* 19 mW power at sample with a minimum of 15 accumulations using an exposure time of 1 s.[24] Spectra were base line corrected (using intelligent fitting with anchored end points) and smoothed (polynomial order 2, smooth window size 7).

Atomic force microscopy (AFM)

A Bruker Dimension FastScan system (Nanodrive V8.36) using PeakForce Tapping mode was used to investigate the morphology of the precursor film in adhesion mode. No sample preparation was required. The resultant images were analysed using ImageJ.

Scanning electron microscopy (SEM)

An Apreo SEM was used to image the precursor HDPE films. Samples were mounted on a stub using double sided carbon tape. A 3 nm layer of gold was added to the surface using a Quorum, Q150 ES plus. The images obtained were analysed in ImageJ.

RG-AEM fabrication

A detailed synthesis method for the preparation of RG-AEMs has previously been reported.[18] To summarise, HDPE films were irradiated using a high energy 10 MeV electron beam (at Sterigenics, Denmark). Samples were irradiated in air using 10 kGy passes until a total absorbed dose of 100 kGy had been achieved. After transport back to Surrey's labs in dry ice, the films were stored in a freezer at −40 ± 2 °C until required.

During the grafting stage, the irradiated films were weighed and immersed in a N_2-pre-purged dispersion of 5% vol VBC (inhibitor removed), 94% vol UPW, and 1% vol 1-octyl-2-pyrrolidone, after which the mixture was purged for a further 1 h at 0 °C. The cold purge allowed sufficient mixing of the grafting solution with the films prior to grafting. To start the grafting reaction the mixture containing the film was moved to a pre-heated water bath (50 °C) and the reaction was left for 4 h with a continuous N_2 flow across the head of the solution. After this grafting process, the grafted samples were washed in toluene and dried overnight in air at room temperature. At this point the mass of the grafted membrane was recorded, and the DoG was calculated (see below).

Subsequently the grafted membranes were submerged in excess aqueous TMA (45% mass) for 24 h. The aminated films (crude RG-AEMs) were then washed in DI water at room temperature, after which they were heated in DI water to 60 °C for 1 h. Ion exchange was completed by immersing the RG-AEMs in aqueous NaCl (1 M) for 1 h (with a minimum of 3 replacements of the solution within this hour). Finally, the RG-AEMs were washed in UPW until no excess Cl^- ions were present, after which they were finally stored in UPW in plastic bottles until required for further characterisation.

Degree of grafting (DoG) calculation

The DoG of the intermediate grafted membrane (before amination) was calculated using eqn (5), where m_i is the mass of the initial HDPE sample (after e^- beaming) and m_g is the mass of the grafted sample after drying.

$$\text{DoG}\ (\%) = \left(\frac{m_g - m_i}{m_i}\right) \times 100 \quad (5)$$

Ion-exchange capacity (IEC) measurements

Each 5 cm^2 RG-AEM sample was dried in a vacuum oven at 50 °C for 4 h before being weighed (m_d) and placed in 20 mL aqueous

$NaNO_3$ solution (2.4 M) for 16 h. The solution was subsequently acidified with 2 mL of aqueous HNO_3 (2 M) and titrated against aqueous $AgNO_3$ (0.02000 – NIST traceable volumetric standard supplied by Thermo Fisher Scientific) using a Titrino plus auto titrator equipped with an Ag-titrode (Cl^- ion selective electrode) and a 5 mL dispensing burette. For each RG-AEM, three replicate samples were analysed for IEC. Prior to using the autotitrator the calibration was checked by titrating blank solutions (three repeats) containing 0.5000 mL of aqueous NaCl solution (0.100 ± 0.004 M) added to 20 mL aqueous $NaNO_3$ solution (2.4 M) and 2 mL of aqueous HNO_3 (2 M); typical endpoint accuracy errors were found to be <1%. The IEC values were calculated using eqn (6), where the endpoint volume (E_p) was taken as the maxima in the first differential plot of Ag electrode potential *vs.* titrant volume.

$$\mathrm{IEC} = \frac{E_p \times [\mathrm{AgNO_3}]}{m_d} \quad (6)$$

Cl^- conductivity measurements

To measure the in-plane Cl^- conductivities, strips of RG-AEM were cut (4 cm × 1 cm) and placed into a BekkTech BT-112 4-probe conductivity test cell (supplied by Alvatek, UK). The cell was submerged in UPW and an alternating current (10 mW amplitude) was applied between 1 Hz and 100 kHz using a Solartron 1260/1287 impedance analyser. Impedance measurements were completed at 25, 40, 60 and 80 °C with the cell left to stabilise at each temperature before the impedance measurement was taken. The low-frequency intercept along the real-axis in the obtained Nyquist plot, was taken as the resistance value (R/Ω). The conductivity (σ/S cm^{-1}) was calculated using eqn (7):

$$\sigma = \frac{l}{R \times w \times t} \quad (7)$$

where l is the distance between the Pt sense electrodes (0.425 cm), and t and w are the thickness and width of the sample, respectively. Replicate measurements were made with $n = 12$ samples for both the treated and untreated RG-AEMs.

Terahertz time-domain spectroscopy (THz-TDS)

The water properties of the AEMs were characterised using the recently reported humidity-controlled THz-TDS.[26] This is an emerging, table-top technique that has demonstrated sensitivity to resolve membrane properties such as water uptake and states, producing results consistent with DVS, DSC and small-angle scattering (X-ray and neutron).[26–28] Samples were prepared into 3 cm × 3 cm size with three repeats for both treated and untreated films. Measurements were acquired in air using a THz-TDS system (TeraSmart, Menlo Systems, Germany) operating between 0.1 and 4 THz on the samples at decreasing relative humidities (RH) of 90, 70, 50, 30, 10 and 0% at steady state at room temperature. An additional data point (labelled 100% RH) was taken at where the sample was analysed immediately from a pre-hydrated state, *i.e.* after removal from UPW immersion with surface water wiped off. A reference measurement was always acquired using the same conditions but without the sample being present; this is to remove water vapor lines and potential pulse drifts. The acquired THz waveforms were then processed to extract film dielectric properties and thicknesses using the previously developed parametric-based algorithm.[29] Using effective medium theory, the water uptakes (WU, percentage mass of water absorbed normalised to the mass of the dehydrated membranes) were then estimated and used with the dielectric properties to estimate proportions of water states as a function of RH.[26]

Fuel cell assembly

The GDEs used in this study were fabricated by hand-spraying catalyst inks onto the Toray GDLs with an Iwata spray gun, using N_2 as the atomizing gas. Each GDE was initially prepared over a 25 cm^2 area, and smaller 5 cm^2 electrodes were cut from the larger electrode for final fuel cell assembly. The measured platinum group metal loadings were approximately 0.73 ± 0.02 mg_{PtRu} cm^{-2} for the anodes and 0.38 ± 0.04 mg_{Pt} cm^{-2} for the cathodes.

The ink formulation was based on previously established protocols, with some modifications.[30,31] For the anode, 45 mg of the ETFE ionomer was ground to reduce agglomerates. It was then combined with 120 mg of PtRu/C, 60 mg of Vulcan XC-72R carbon, and 18 mg of PTFE powder, followed by further grinding to homogenise. 1.5 mL of UPW was gradually added, after which 11 mL of IPA was introduced in four increments under continuous manual grinding until a uniform, low-viscosity slurry was obtained. The resulting dispersion was transferred to a LDPE vial and sonicated in an ice-bath ultrasonicator (Fisher Scientific FS30H) for 60 min. The cathode ink was prepared in a similar manner, using 25 mg of the ETFE ionomer, 100 mg of Pt/C, 1 mL of DI water, 7 mL of IPA, and 10 mg of PTFE powder.

Before assembling each MEA, the electrodes and AEM were immersed in aqueous KOH (1.0 M) for 1 h, with solution refreshed every 20 min, to ensure complete ion exchange from the Cl^- to the OH^- forms. After thoroughly removing excess alkali, the membrane was sandwiched between the electrodes and mounted into a Scribner single-cell fixture without hot pressing. The cell hardware employed 5 cm^2 single-channel serpentine flow fields. Considering the measured GDE thicknesses (*ca.* 209–220 μm), 6 mil thick Teflon gaskets were used on both sides, achieving an estimated compression of 25%.

Fuel cell testing

Following assembly, each fuel cell was operated using a Scribner 850e test station. Initially, N_2 was supplied to both anode and cathode sides at a flow rate of 0.4 L min^{-1} while the cell was brought to the target temperature. The humidifier setpoints were maintained at 60 °C, and the cell temperature was gradually increased to ensure it remained below the humidifier temperatures throughout the warm-up process to avoid dry-out, thereby keeping the membrane at a proper hydration state. Once the cell temperature reached 60 °C, the break-in procedure was initiated by switching the gas feeds at the anode and cathode to H_2 and O_2, respectively. The system was held at open circuit until a stable open circuit voltage (OCV) was achieved. Subsequently, a gradual voltage decrease from OCV to 0.1 V was applied to activate the cell and facilitate the removal of residual

carbonate species (formed during air exposure of the OH^--exchanged RG-AEM and electrodes) as CO_2. After break-in, the cell temperature was increased to 80 °C, again ensuring that the humidifier temperatures were always greater than or equal to the cell temperature. The cell was then set at a constant voltage of 0.6 V and gas flow rates of 1 L min^{-1}. Following this, the dew points of the feed gases were systematically adjusted either to achieve a desired operating condition or to optimise cell performance. Polarisation curves were recorded by sweeping the cell voltage from OCV down to 0.1–0.2 V at a rate of 10 mV s^{-1}. Throughout all measurements, the high-frequency resistance (HFR) of the cell was continuously monitored using the built-in impedance measurement capabilities of the Scribner 850e system, equipped with an 881 Frequency Response Analyzer (FRA) operating at 7 kHz.

Results and discussion

Crystallinity of precursor film (treated and untreated)

An initial objective of this study was to develop a thermal treatment method which could be applied to a precursor commercial HDPE film to reduce crystallinity variation. For the following measurements, HDPE film samples were heated in the oven for 24 h at different temperatures and then naturally cooled (*i.e.* oven switched off and left for 24 h); this was followed by the measurement of crystallinities using DSC (Fig. 1). Spatially adjacent samples of the film on the HDPE roll were untreated and treated to ensure a fair crystallinity comparison (as it is known that the crystallinity of untreated HDPE can vary over longer distances).[18] To maintain a uniform film thickness of 10 μm (an advantage of radiation grafting is that commercial films of controlled thickness are modified), the treatment temperatures were maintained below the melting point of HDPE (130.9 °C ± 1.1 °C). Zhang *et al.* have shown that low temperature treatment of PE (<100 °C) can cause lamella growth, with the dominant growth mechanism dependent on the treatment temperature.[32] At a treatment temperature of 57 °C, chain sliding was shown to be the dominant lamella growth mechanism, where polymer chains slide to allow adjacent lamellae to fuse and thicken. At a treatment temperature of 87 °C, melt recrystallisation (the process of unstable smaller crystallites melting and reforming on stable existing nuclei), was the dominant growth mechanism.[32,33]

Fig. 1(a) shows the change in crystallinity (DSC measurement) of the HDPE films after thermal treatment at 50, 85, and 115 °C for 24 h. The slight increase in crystallinity at 50 °C is likely a result of chain sliding, whilst the melt recrystallisation method is the most probable cause of increased crystallinity at 85 and 115 °C. The HDPE film treated at 115 °C showed the largest increase in crystallinity, a result of the treatment temperature being closer to the melting temperature thus allowing increased mobility of the polymer chains. It was confirmed *via* thickness measurements that no thinning of the precursor film took place during the thermal treatment process.

Fig. 1(b) shows the DSC endothermic melting peaks obtained after HDPE samples were treated at 50, 85, and 115 °C. At 115 °C, the DSC onset melting temperature increased from *ca.* 105 °C to *ca.* 116 °C, which is consistent with the minimum crystallite sizes increasing on thermal treatment. The melting peaks of the thermally treated films were also broader compared to the untreated precursor film controls, which is a consequence of partial recrystallisation during cooling leading to an increased variation in lamellae thicknesses. Strobl *et al.* have argued that upon cooling, partial crystallisation occurs causing thinner lamellae to form in the amorphous regions located between thicker lamellae.[34] A shoulder in the melting peak was also observed for the treated films, this became more pronounced at higher treatment temperatures with multiple peaks seen for some measurements. Multiple endothermic peaks in the DSC of PE have previously been reported in the literature, a consequence of the presence of multiple distributions of lamellae thicknesses.[35,36]

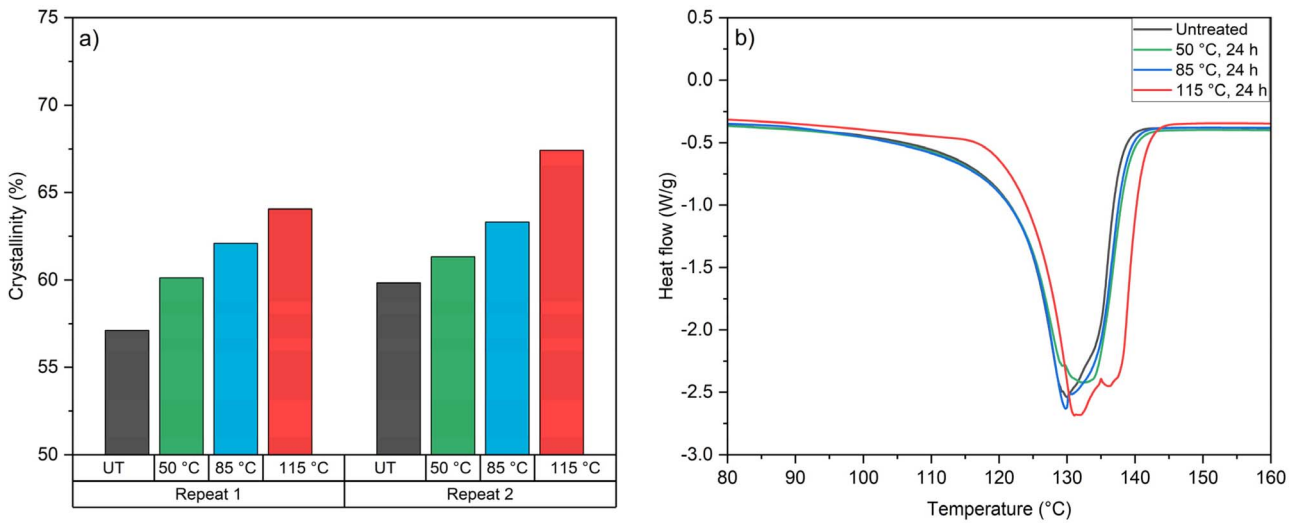

Fig. 1 (a) The crystallinity of PE film calculated using DSC when left untreated (UT) and when treated in an oven for 24 h at 50, 85 and 115 °C. After treatment, the samples were cooled naturally in the oven. This measurement was repeated twice at two separate locations of the commercial PE roll. (b) The endothermic melting peaks obtained from DSC (repeat 2) in a heat cool cycle after thermal treatment of the PE films.

A shorter treatment time would be amenable for future RG-AEM scale-up as it would reduce the total manufacturing time. Consequently, a 2 h thermal treatment time was investigated for each proposed treatment temperature, this did not result in observable differences in crystallinity or noticeable changes to the melting peak (SI Fig. S1). As the 24 h thermal treatment at 115 °C resulted in the greatest increase in crystallinity compared to the pristine HDPE film (an objective of this study), this thermal treatment method was selected for further investigation.

To determine if the crystallinity variation within the precursor film was reduced after applying thermal treatment, a 60 × 15 cm section of film was treated (designated T), whilst an adjacent section of equivalent size on the HDPE roll remained untreated (designated UT). Density measurements were then undertaken on samples, as this is the most reliable way to measure bulk crystallinities.[24] This was repeated at three spatially separated locations along the HDPE roll. Fig. 2 shows that at each location, thermal treatment increased the mean crystallinity of the film (95% confidence level, two sample *t*-test with Welch correction, $p = 6 \times 10^{-4}$, combined data from all locations) and successfully reduced the spread of degree of crystallinity values (two sample *F*-test showed the variance of UT and T samples were significantly different, $F(17, 14) = 3.85$, $P = 0.007$, 95% confidence level).

DSC and density measurements are both techniques that measure bulk crystallinity, albeit using different sample sizes and calculation methods, which can yield differing crystallinity values on the same sample.[24] For additional insights, Raman spectroscopy was used to map the surface crystallinity of the treated and untreated HDPE samples at micron-level spatial resolution. A 20 × 20 μm area was mapped and the crystallinity calculated using eqn (3); this was repeated in three spatially different locations for both untreated and treated samples. Fig. 3 shows an example of the resulting maps, which clearly show an increase in crystallinity. An 'hour glass' multimodal distribution is observed in the box plots of the three mapping areas recorded on the untreated HDPE, indicating equivalent sized regions of high and low crystallinity; the narrower middle section is indicative of the intermediate phase which occurs at the crystalline-amorphous boundary.[24] The distributions shift to higher mean crystallinities upon thermal treatment: 86% mean compared to 77% for the untreated film. This data is indicative of a change in the microstructure at the surface of the HDPE. These surface degree of crystallinities are intermediate to the bulk 89% (T) and 84% (UT) overall means recorded using density measurements, and the 66% (T) and 58% (UT) values recorded using DSC, as observed before.[24]

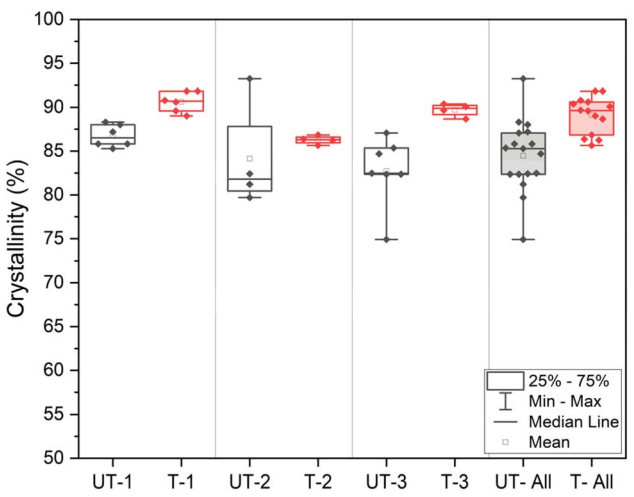

Fig. 2 The degree of crystallinity of HDPE film samples determined from density measurements where the treated samples (115 °C for 24 h and then cooled naturally in the oven over 24 h) were directly adjacent to the corresponding untreated control samples. Measurements were recorded at three widely spatially separated locations along the HDPE roll with $n = 4$–6 repeat measurements at each location. The box plots for the combined data are also given on the right of the plot (shaded).

SEM and AFM are powerful imaging techniques that can be used to observe crystallinity at the sub-μm resolution. In polymers, AFM can be used to distinguish between crystalline and amorphous regions by measuring stiffness at the surface; crystalline regions exhibit a stiffer surface whilst amorphous regions show greater elasticity.[37,38] Fig. 4(a) shows an AFM image of the untreated precursor film, where amorphous channels (between 0.8 and 2 μm) separate the crystalline domains that contain lamellae that are orientated perpendicular to the channels. The orientation of polymer features is dependent on the processing conditions, which are typically withheld by suppliers.[39] The SEM images of the untreated precursor film (note: not the same locations as the AFM locations) also show clear orientation of the lamellae (Fig. 4(c)). In Fig. 4(c) a large (*ca.* 6 μm wide) amorphous section can be seen to cut through the crystallite domains. The size of the amorphous regions in both AFM and SEM micrographs are comparable to those observed in the Raman crystallinity maps.

Post treatment, the orientational order within the precursor film decreases; this is more obvious with the SEM images (Fig. 4(d)) where some lamellae are observed to be angled away from a predominant orientation. Furthermore, the amorphous channels were smaller and not as distinct, which is consistent with the increased surface crystallinities measured using Raman microscopy. A reduction in orientational order of the thermally treated film is reasonable as no external force was applied to the film during thermal treatment. In the AFM micrographs of the treated film (Fig. 4(b)), large regions of ordered lamellae are observed that are similar to that seen with the untreated film, but lamellae of different thickness are also observed at the interface of the crystalline and amorphous regions. Fig. 5 gives a histogram of lamellae widths estimated using both AFM and SEM for the treated (dashed line) and untreated (solid line) HDPE films. A larger average and broader distribution of lamellae widths was observed for the thermally treated film compared to the untreated benchmark; this is in agreement with the higher onset melting temperature and broader endothermic melting peak observed in the DSC for the treated film.

In summary, thermal treatment at 115 °C for 24 h (followed by natural cooling in the oven) increases the degree of crystallinity of the HDPE film, with less orientated, wider lamellae, and

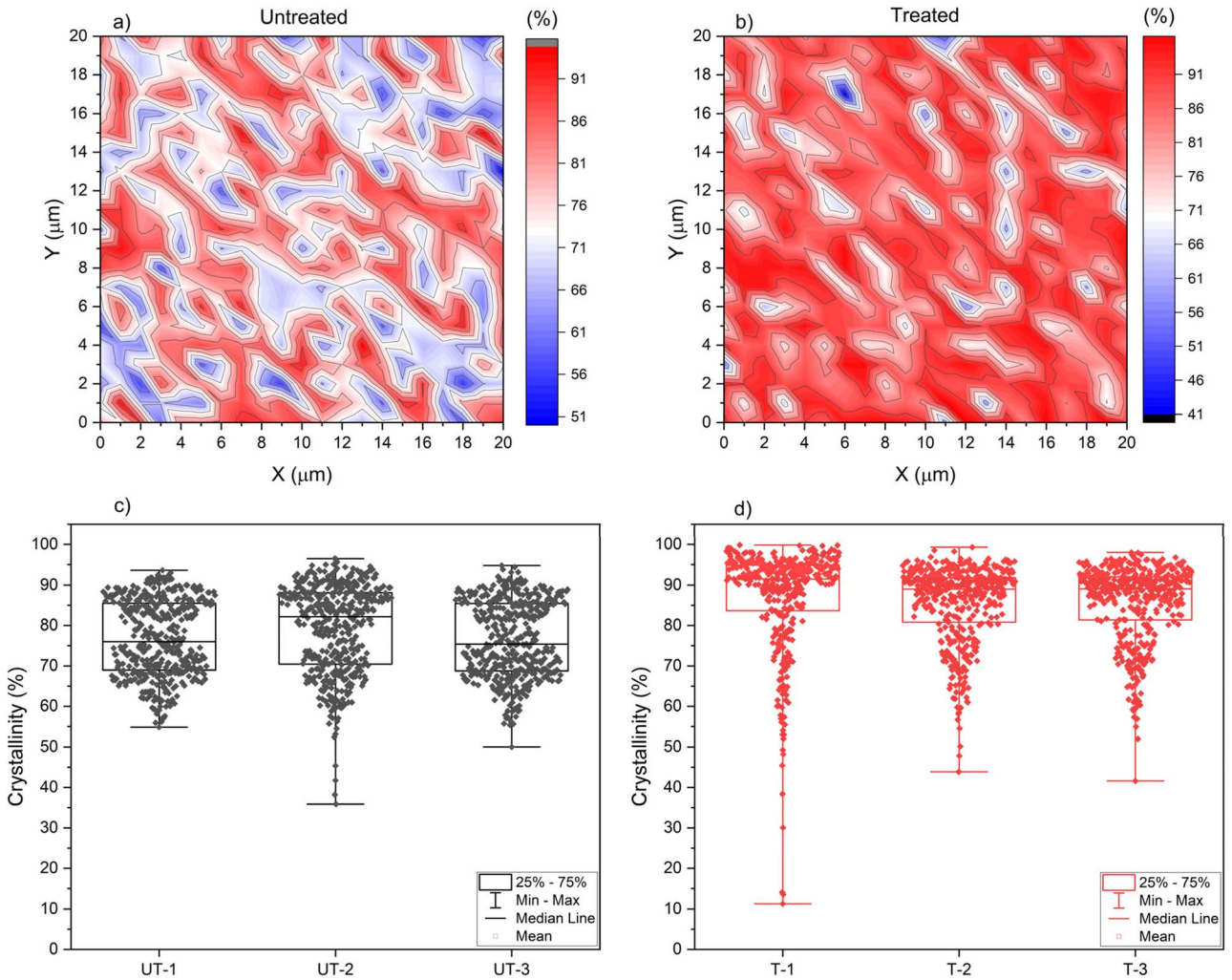

Fig. 3 (a) An exemplar crystallinity map showing the change in crystallinity (calculated using Raman spectroscopy) over a 20 μm × 20 μm sampling area of untreated HDPE film. (b) Crystallinity map of a 20 μm × 20 μm area of a HDPE film that has been thermally treated at 115 °C for 24 h. (c and d) Corresponding box plots showing the range of crystallinity values calculated over 3 spatially separated 20 μm × 20 μm sample areas of the untreated (UT) and thermally treated (T) HDPE film samples, respectively.

a decrease in amorphous domain size. Importantly, the thermally treated HDPE substrate film exhibited mean degrees of crystallinity that average more than 81% threshold, a threshold that our prior study indicated was important for fabricating RG-AEMs with more consistent properties.[18]

Properties of the RG-AEMs fabricated from the HDPE films

To make AEMs, a 20 cm × 60 cm section of film, cut lengthways down the commercial roll, was thermally treated. An adjacent section of film sharing the same 60 cm boundary was left untreated (as shown in SI Fig. S2). Both samples were cut into 12 sets of 10 cm × 10 cm squares before irradiation; the films were subsequently grafted with VBC monomer. The VBC-grafted samples made from the thermally treated HDPE substrate gave a DoG of (185 ± 23)%, compared to (171 ± 15)% for the those made from the untreated HDPE ($n = 12$ repeats for each). The DoG values calculated for the bulk film samples (using eqn (5)) were found not to be statistically different (95% confidence interval, two sample t-test, $p = 0.07$), but this is primarily due to the measurement errors involved (low mass, <100 mg, samples being weighed with clear static electrical interferences).

Fig. 6(a) shows the average Raman spectra of the grafted samples (averaged response over $n = 2$ Raman measurements on the surface of each square of each sample). The bands at 1000 cm^{-1}, 1268 cm^{-1} and 1612 cm^{-1} correspond to aromatic ring breathing, CH_2–Cl groups and the aromatic ring quadrant mode of poly(VBC) respectively. Combined, these confirm that grafting has successfully occurred (dashed lines in Fig. 6(a)).[28,40] The integrated area ratio of the monomer peak at 1612 cm^{-1}, normalised to the HDPE C–C asymmetric stretching peak at 1063 cm^{-1}, was used to measure the homogeneity of grafting (Fig. 6(b)). The treated precursor film had a larger mean area ratio (4.9 ± 0.5) compared to the untreated film (4.7 ± 0.5), indicating a slight increase in the degree of grafting on thermal treatment; a two sample t-test (95% confidence interval) showed that the difference in the mean Raman band area ratio was statistically significant ($p = 0.02$). A higher DoG for the more crystalline treated film initially appears counter intuitive as it is

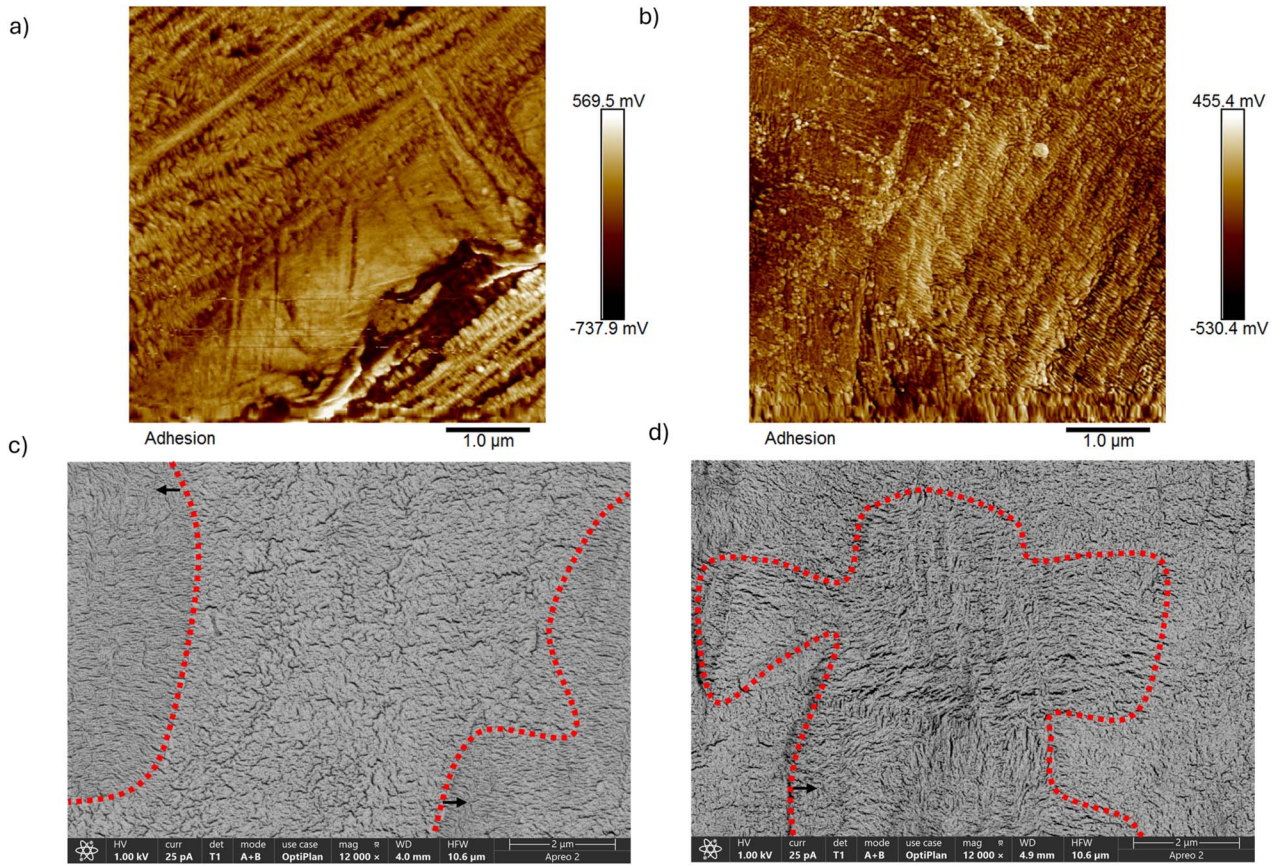

Fig. 4 (a) AFM image of the untreated HDPE precursor film where the lamellae appear orientated in one direction. (b) AFM image of a thermally treated (115 °C for 24 h) HDPE sample. (c and d) Give the SEM images of untreated and thermally treated precursor films, respectively, where the crystallite domains are highlighted inside the red zones.

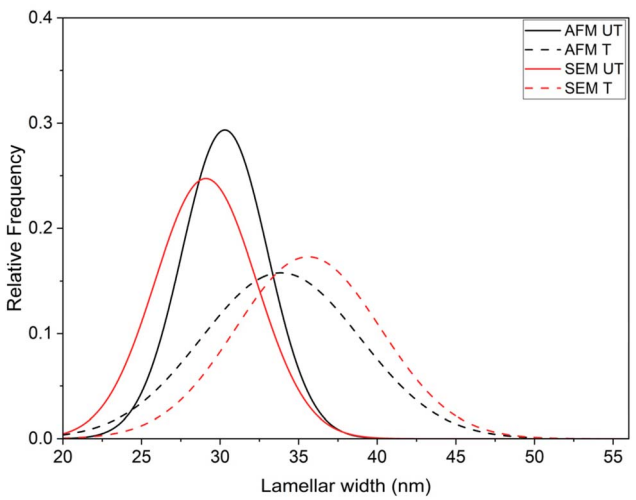

Fig. 5 Histogram of measured lamella widths estimated from AFM (black) and SEM (red) measurements, where the dashed lines represent the thermally treated (115 °C, 24 h) HDPE film (T) and the solid line indicates the untreated benchmark HDPE film (UT). The total number of sample lamella analysed was 289, 148, 195 and 186 for AFM UT, AFM T, SEM UT and SEM T, respectively.

known that grafting primarily occurs in the amorphous domains.[41] It is necessary, however, to take into account the change in lamella size and orientation (SEM and AFM data in Fig. 4 and 5), both of which would impact the rate of the grafting reaction. Our observation is consistent with the prior observations of Sproll *et al.*, who looked at grafting styrene onto ETFE substrates with different crystallinities.[12] They showed that the ETFE substrate with larger crystallites (from DuPont) yielded more efficient grafting. The VBC-grafted membrane made from the higher crystallinity (thermally treated) HDPE in our study has larger mean crystallite sizes (see above) so a higher level of grafting would be expected.

Fig. 7(a) shows the resultant Raman spectra of the final aminated RG-AEMs. The absence of the 1268 cm^{-1} CH_2–Cl grafted band and the appearance of the quaternary ammonium head group band at 979 cm^{-1} demonstrates successful amination (see dashed lines in Fig. 7(a)).[17,18] Titrations were completed on each of the 12 samples (3 repeats per sample). A statistically higher (at 95% confidence level, two sample *t*-test, $p = 0.03$) mean IEC of 2.8 mmol g^{-1} was measured for the AEM prepared using the treated precursor film compared to 2.7 mmol g^{-1} for the untreated counterpart. This corroborates the higher DoG for the grafted (pre-aminated) membranes fabricated from the treated precursor HDPE film as the number

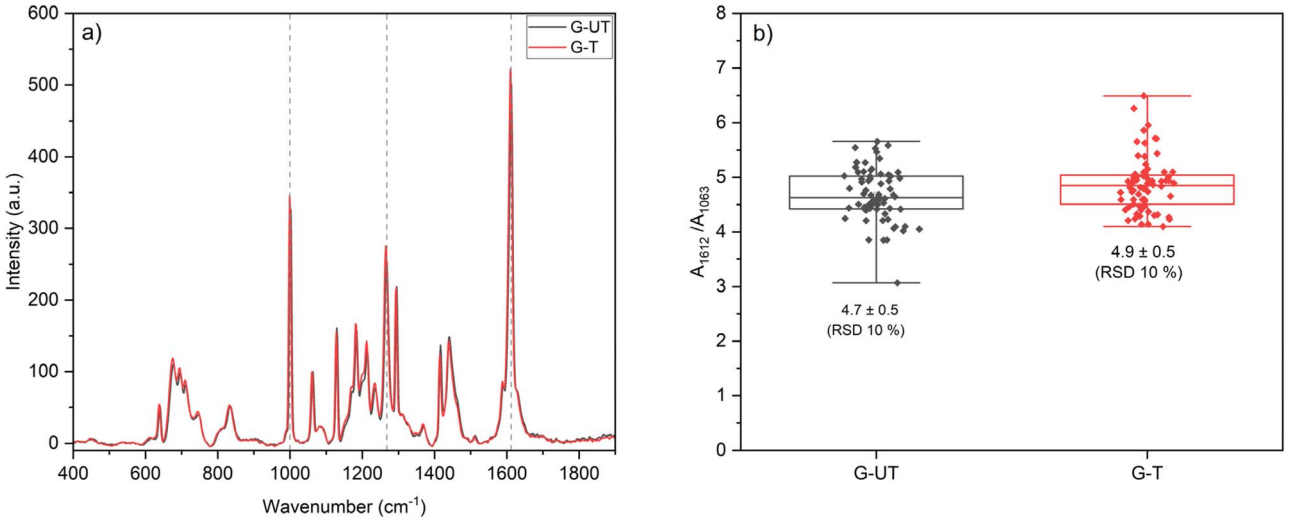

Fig. 6 (a) Raman spectra of the poly(VBC)-grafted membranes fabricated from both the untreated and thermally treated (115 °C, 24 h) HDPE precursor films (labelled G-UT and G-T, respectively). Each spectra is an average of 24 spectra, collected over $n = 2$ repeat Raman measurements on each of the $n = 12$ grafted membrane samples. (b) A box plot measure of the grafting homogeneity showing the integrated area ratios of the poly(VBC) band at 1612 cm^{-1} normalised to the HDPE band at 1063 cm^{-1} ($n = 60$).

of grafted functional poly(VBC) groups (DoG) is expected to directly result in the number of quaternary ammonium groups that are present in the final RG-AEMs (IEC).[42] As shown in the box plot in Fig. 7(b), the variation in the IEC measurements was smaller for the AEMs with the treated precursor films. This suggests that reducing the natural crystallinity variation in the precursor film impacted the synthesis of the RG-AEMs and reduced variation in the resultant IEC values; this is a useful result when considering potential future scale up of RG-AEM production.

AEMFC performances are greatly impacted by an AEM's relationship with water and its ionic conductivity. Fig. 8(a) shows the gravimetric WU of the AEMs between 0% RH and full hydration (denoted as 100% RH). Above 70% RH, an increase in WU was observed for the RG-AEM samples prepared using the treated precursor film. THz-TDS separates the water states in AEMs into bulk, bound and free (Fig. 8(b)). Bound water predominately consists of water molecules that are interacting strongly with the hydrophilic head groups (polar and hydrogen bond interactions). Bulk water refers to the water in the hydrophilic channels (having lower levels of interactions with the polymer) and are able to undergo rearrangement, which underpins ionic conduction.[43] The AEMs with the treated precursor films showed a greater portion of bulk water (66 ± 7% when fully hydrated) compared to their non-treated counterparts (58 ± 4%). An increased portion of bulk water is indicative of improved ionic conductivity (the slight increase in conductivity in Fig. 9 for the RG-AEM made from the thermally treated

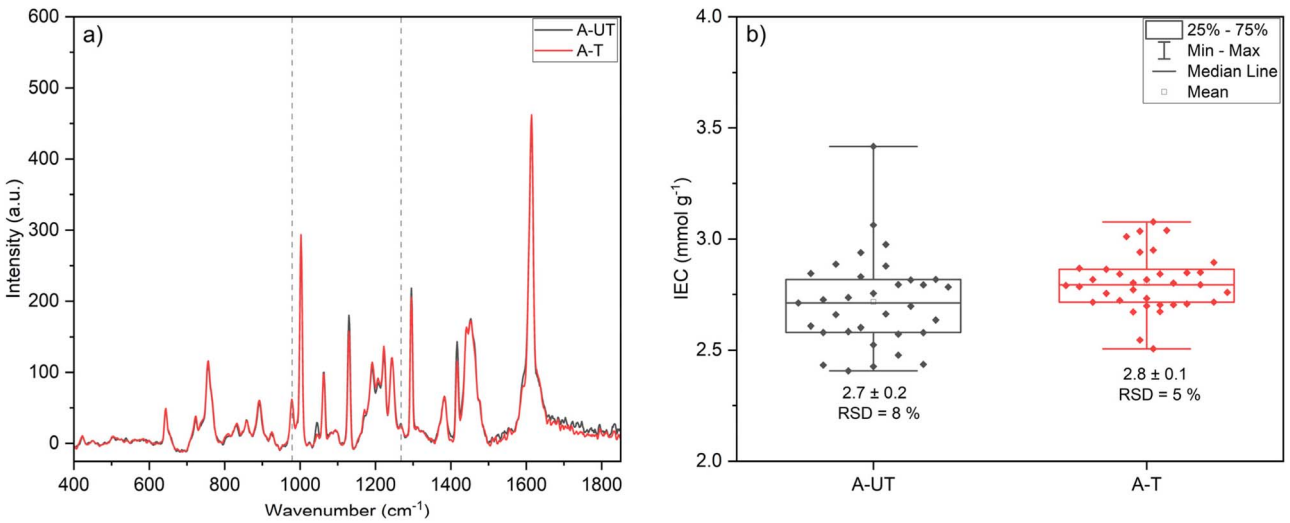

Fig. 7 (a) Raman spectra of the aminated RG-AEMs fabricated from both the untreated and thermally treated (115 °C, 24 h) HDPE precursor films (labelled A-UT and A-T, respectively). (b) A box plot measure of the IEC homogeneity from titrations on $n = 12$ RG-AEM samples (with $n = 3$ repeats on each sample) made from both the treated and untreated HDPE films.

HDPE). Finally, free water refers to water that is not bound to the ionic hydration shell and that does not significantly contribute to anion mobility.[44]

It was commonly believed that free water is essential for fast ion transport using the vehicular transport mechanism. Recent work by Pablo *et al.*, however, has shown that fast ion transport is instead enabled *via* the formation of robust water networks within the AEM (bulk water is more relevant for this).[45,46] As can be seen in Fig. 8(b), there is no perceptible change in the percentage of free water in the AEMs at all RHs; this is encouraging as it suggests thermal treatment of the precursor film is changing the hydration network without the addition of excess "non-useful" water that can contribute to excessive swelling and mechanical weakening of the membrane.

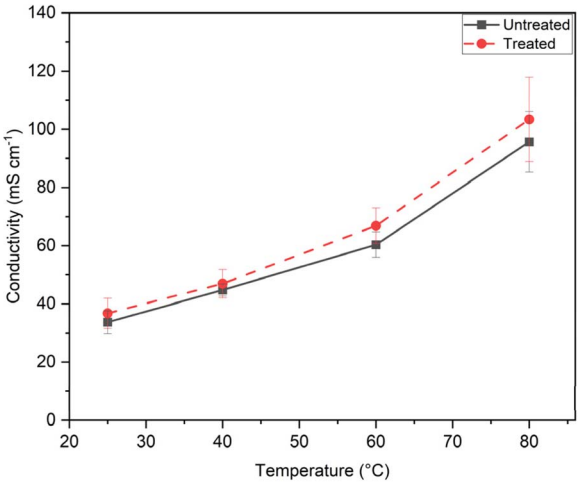

Fig. 9 In-plane Cl^- conductivities of RG-AEMs prepared with the treated (24 h at 115 °C, red) and untreated (black) precursor HDPE films; the samples were fully hydrated and submerged in UPW. The average conductivity (where $n = 12$ separate measurements) is plotted with standard deviation shown as error bars.

Anion exchange membrane fuel cell (AEMFC) performance

Fig. 10(a) directly compares the performance of the RG-AEMs, with the treated and untreated precursor film, in a H_2/O_2 AEMFC test where all other variables (cell hardware, gas flow rate, humidification and back pressure) were kept constant. Fuel cell testing was conducted at a cell temperature of 80 °C with relatively well hydrated gas supplies (anode dew point set to 73 °C and the cathode dew point over hydrated to 81 °C). A backpressure of 100 kPa was applied to both gas feeds. Under these conditions, the cell containing the RG-AEM with the untreated precursor film was able to achieve a peak power density (PPD) of 2.0 W cm^{-2}. The limitation in the PPD was the sharp decline in cell voltage, power density and HFR at a current density of approximately 5.7 A cm^{-2}, all characteristic of significant flooding. The cell containing the RG-AEM made from the thermally treated HDPE was able to achieve a slightly higher PPD of 2.1 W cm^{-2} (albeit limited by an earlier onset of flooding at *ca.* 3.3 A cm^{-2}); it also outperformed the benchmark RG-AEM in the voltage range of 0.6–0.8 V, which is relevant for practical operation in industry. This enhancement is attributed to lower ohmic losses, as evidenced by reduced HFR values throughout the test. These observations correlate well with the higher ionic conductivity, IEC, and bulk water uptake measured for the RG-AEM made from the treated HDPE, which all suggests further potential performance increases can be obtained on further optimisation of the operating dew points.

Fig. 10(b) presents the optimised performance data where the anode and cathode dew points were systematically adjusted under constant voltage operation (0.6 V) to find the conditions with the highest operating current. Interestingly, both cells achieved an identical maximum PPD of 2.84 W cm^{-2} (even superior to the highest performance of 2.55 W cm^{-2} previously reported for HDPE-based RG-AEM in our earlier work).[17] However, the optimal operating conditions for these two

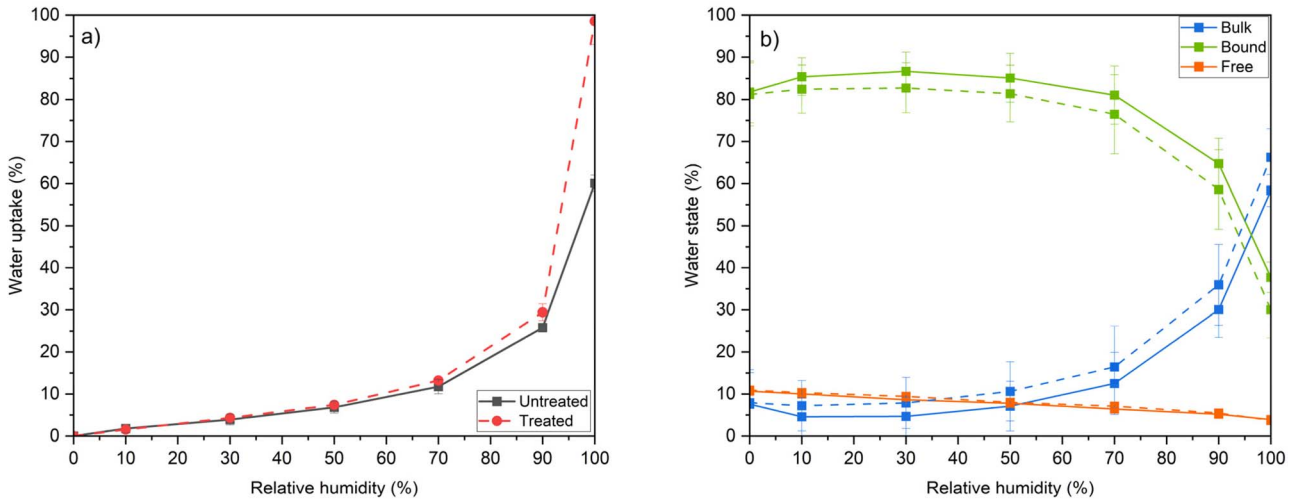

Fig. 8 (a) Gravimetric WU values of RG-AEMs prepared using untreated and treated (115 °C, 24 h) HDPE precursor films when exposed to increasing levels of humidities (note "100% RH" is where the RG-AEM samples were removed from water immersion and surface water quickly removed). (b) THz-TDS data showing the different proportion of water states in the membrane at varying RH (solid = untreated, dashed – treated).

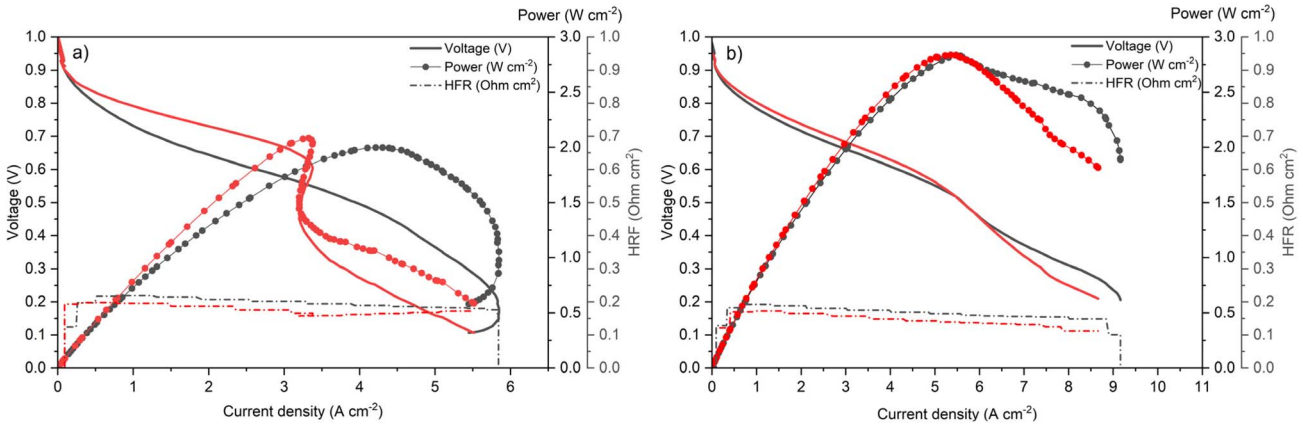

Fig. 10 (a) A direct H_2/O_2 AEMFC performance comparison of the RG-AEMs made from the treated (red lines) and untreated (black lines) HDPEs. A cell temperature of 80 °C was used with the anode dew point set at 73 °C and the cathode dew point set at 81 °C (back pressures of 100 kPa used for both gas supplies). (b) Performances with optimised operating conditions: anode/cathode dew points of 63/70 °C and 72/77 °C for the RG-AEMs made from the treated and untreated HDPE, respectively (back pressures for both RG-AEMs of 100 kPa for H_2 and 150 kPa for O_2). All current sweeps were in the forward direction (from OCV to high currents) at 10 mV s^{-1} for these quick beginning-of-life performance tests.

membranes differ significantly, and these differences directly reflect the superior practical performance of the treated RG-AEM under industrially relevant conditions. For the RG-AEM made from the treated HDPE, the optimised anode and cathode dew points were 63 °C at the anode and 70 °C at the cathode, while the optimised PPD for the benchmark RG-AEM these values were 72 °C and 77 °C, respectively. The differences in the optimised dew points clearly show the enhanced ability of the RG-AEM made from the treated HDPE to uptake water, requiring lower dew points to maintain sufficient hydration, along with the lower observed HFR values. This behaviour indicates that the treated RG-AEM is more tolerant to dry-out, a critical advantage because insufficient hydration can lead to irreversible degradation during practical operation. The combination of the polarisation behaviour and the HFR suggests that the water state of the cell is dynamically changing during the experiment. This is especially notable at the highest currents where the HFR was very low, likely due to flooding at the anode as the RG-AEMs are unable to uptake anode-generated water molecules and transport them to the cathode quickly enough. Lastly, consistent with earlier results, the cell with the RG-AEM made from the treated HDPE maintained higher operating currents at intermediate voltages (2.7 A cm^{-2} at 0.7 V *cf.* 2.1 A cm^{-2} for the untreated RG-AEM, under optimised operating conditions). Since the industrial operating window is 0.6–0.8 V, this directly contributes to more robust and commercially relevant performance. Collectively, these results highlight the advantages of HDPE thermal treatment in improving the connected hydrophilic network of the RG-AEMs and its practical applicability.

On longer-term fuel cell operation, the polymer chains could well move (affecting crystallinity), and this may affect longer-term *in situ* performances. This certainly needs to be studied in the future. Recall, the main point of the paper was to look at HDPE substate crystallinity effects on DoG, IEC, conductivity, and water uptake properties. We simply included fuel cell data to give an initial relative comparison of *in situ* fuel performances to probe if the higher water uptake and conductivities observed (with the thermally treated HDPE substrate) would lead to more optimal beginning-of-life fuel cell performance characteristics.

Conclusions

The degree of crystallinity of high-density polyethylene (HDPE) was altered *via* thermal treatment. A treatment temperature of 115 °C for 24 h was found to result in the highest increase in crystallinity, whilst still having the advantage of keeping the temperature below the melting point of HDPE. Differential scanning calorimetry and density measurements showed that the bulk crystallinity of HDPE increased and the variation between samples decreased after thermal treatment, whilst Raman spectroscopy showed micrometre increases in the crystalline domain sizes on the surface of the thermally treated HDPE. Scanning electron microscopy and atomic force microscopy showed that thermal treatment increased the lamellae size distributions, but reduced the orientational order within the film.

Upon radiation-grafting and amination (using vinylbenzyl chloride monomer and trimethylamine) of the treated and untreated precursor HDPE films, it was found that the HDPE treatment led to a radiation-grafted anion-exchange membrane (RG-AEM) with a higher ion-exchange capacity (IEC). Furthermore, the variation in IEC was lower; this is advantageous as RG-AEMs with consistent properties are mandatory when considering scale up.

The interaction of the RG-AEMs with water was found to change upon thermal treatment of the precursor HDPE film. Above 70% relative humidity, a dramatic increase in WU occurred with thermal treatment. Terahertz-time-domain spectroscopy (THz-TDS) was used to further investigate the water states present within the RG-AEMs. It was shown that the proportion of bulk water increased with the RG-AEMs made with the treated HDPE (compared to the untreated benchmark), which was supported by an improvement in in-plane

conductivity. The optimised (made from thermally treated HDPE) RG-AEM's improved ability to uptake and transport water was also observed during fuel cell testing with the optimum dew points for the treated AEM being considerably lower (63 °C anode and 70 °C cathode) compared to the untreated RG-AEM (72 °C anode and 77 °C cathode). The improved conductivity of the optimised RG-AEMs also resulted in a lower *in situ* HFR values being observed during testing.

Overall, this paper has highlighted the importance of controlling the crystallinity of the precursor films in the fabrication of and properties of optimised RG-AEMs, in particular the AEM's ability to interact with water. Further work is needed to fully understand how the lamellae orientation and crystallite size affect the grafting reaction and consequently the water transport ability of the RG-AEMs.

Author contributions

The membrane fabrication and film/membrane property experiments (DSC, SEM, AFM, density, Raman, IEC and conductivity) were all conducted by Siân Franklin. The water uptake and THZ-TDS measurements were conducted by Mozhdeh Mohammadpour Zehaab, while the fuel cell tests were conducted by Yingdan Cui. Siân Franklin drafted the bulk of the manuscript, with the assistance of Mozhdeh Mohammadpour and Yingdan Cui (providing text on their techniques). All authors assisted with data analysis and provided comments and corrections to the draft manuscript.

Conflicts of interest

There are no conflicts to declare.

Data availability

The raw data behind the figures are available under a CC-BY open access licence at DOI https://doi.org/10.6084/m9.figshare.30316660.

Supplementary information (SI): additional SEM data and a diagram of sampling methods. See DOI: https://doi.org/10.1039/d5ta08440g.

Acknowledgements

Siân Franklin's PhD fees and stipend were kindly funded by AFC Energy PLC. The HDPE films and other lab consumables used were provided by funds from the UK' Engineering and Physical Sciences Research Council EPSRC grant EP/T009233/1. The Renishaw Raman instrument was funded on EPSRC grant EP/M022749/1, while the THz-TDS work was funded by EPSRC grant EP/Z534237/2. Mozhdeh Mohammadpour acknowledges School of Engineering at Lancaster University and Johnson Matthey for an international PhD studentship. The THz team additionally acknowledges technical support from Mr George France. Funds to support the time commitment for Yingdan Cui and William Mustain were provided by Plug Power Inc.

References

1 C. Li and J. Baek, *Nano Energy*, 2021, **87**, 106162.
2 M. L. Jordan, T. Kulkarni, D. I. Senadheera, R. Kumar, Y. J. Lin and C. G. Arges, *J. Electrochem. Soc.*, 2022, **169**, 043511.
3 G. H. A. Wijaya, K. S. Im and S. Y. Nam, *Desalin. Water Treat.*, 2024, **320**, 100605.
4 K. Yassin, I. G. Rasin, S. Brandon and D. R. Dekel, *J. Membr. Sci.*, 2024, **690**, 122164.
5 C. G. Arges, V. Ramani and P. N. Pintauro, *ECS Interface*, 2010, **19**, 31.
6 Y. Zhao, K. Yoshimura, A. Radulescu and Y. Maekawa, *Macromolecules*, 2025, **58**, 663.
7 M. Rezayani, F. Sharif and H. Makki, *J. Mater. Chem. A*, 2022, **10**, 18295.
8 C. W. Johnson, L. Zhang, K. E. Culley, S. M. Oh, D. L. Gin, G. M. Geise, A. J. Patel, K. I. Winey and C. O. Osuji, *ACS Nano*, 2025, **19**, 2559.
9 H. Lim, J. Jeong, D. H. Lee, S. Myeong, G. Shin, D. Choi, W. B. Kim, S. M. Choi and T. Park, *J. Mater. Chem. A*, 2023, **11**, 25938.
10 L. Fischer, S. S. Hartmann, A. Maljusch, C. Däschlein, O. Prymak and M. Ulbricht, *J. Membr. Sci.*, 2023, **669**, 121306.
11 W. Lee, E. J. Park, J. Han, D. W. Shin, Y. S. Kim and C. Bae, *ACS Macro Lett.*, 2017, **6**, 566.
12 V. Sproll, G. Nagy, U. Gasser, J. P. Embs, M. Obiols-Rabasa, T. J. Schmidt, L. Gubler and S. Balog, *Macromolecules*, 2016, **49**, 4253.
13 A. Chakraborty, I. Salam, M. Choolaei, J. Lee, C. Crean, D. K. Whelligan, R. Bance-Soualhi and J. R. Varcoe, *Mater. Adv.*, 2023, **4**, 2099.
14 J. Lee, K. Min, S. Jeon, S. Park, H. Kim and T. Kim, *Int. J. Hydrogen Energy*, 2023, **48**, 24180.
15 J. Ponce-Gonzalez, I. Ouchan, J. R. Varcoe and D. K. Whelligan, *J. Mater. Chem. A*, 2018, **6**, 823.
16 A. S. Barbosa, A. G. Biancolli, A. J. C. Lanfredi, O. Rodrigues Jr, F. C. Fonseca and E. I. Santiago, *J. Membr. Sci.*, 2022, **659**, 120804.
17 L. Wang, X. Peng, W. E. Mustain and J. R. Varcoe, *Energy Environ. Sci.*, 2019, **12**, 1575.
18 S. A. Franklin, C. Crean and J. R. Varcoe, *RSC Appl. Polym.*, 2026, DOI: 10.1039/D5LP00277J.
19 A. G. Bianoclli, D. Herranz, L. Wang, G. Stehlikova, R. Bance-Soualhi, J. Ponce-Gonzalez, P. Ocon, E. A. Ticianelli, D. K. Whelligan, J. R. Varcoe and E. I. Santiago, *J. Mater. Chem. A*, 2018, **47**, 24330.
20 S. D. Poynton, R. C. T. Slade, T. J. Omasta, W. E. Mustain, R. Escudero-Cid, P. Ocon and J. R. Varcoe, *J. Mater. Chem. A*, 2014, **14**, 5124.
21 W. Lin, M. Cossar, V. Dang and J. Teh, *Polym. Test.*, 2007, **26**, 814.
22 R. L. Blaine, *Thermal application notes*, TA Instruments, 2002, TN048, pp. 1–2.
23 Z. Bartczak, *Polym. Test.*, 2018, **68**, 261.
24 S. A. Franklin, H. Herman, R. Bance-Soulalhi, C. Crean and J. R. Varcoe, Raman microscopy of high-density

polyethylene: rapid mapping of crystallinity domains at the μm spatial resolution, 2025, DOI: 10.6084/m9.figshare.28816238.
25 W. H. Lee, C. Crean, J. R. Varcoe and R. Bance-Soualhi, *RSC Adv.*, 2017, **7**, 47726.
26 G. A. H. Ludlam, S. J. P. Gnaniah, R. Degl'Innocenti, G. Gupta, A. J. Wain and H. Lin, *ACS Sustainable Chem. Eng.*, 2024, **12**, 7924.
27 G. A. H. France, M. Mohammadpour, R. Degl'Innocenti, M. Peruffo and H. Lin, *IEEE Trans. Terahertz Sci. Technol.*, 2025, **15**, 743.
28 T. R. Wilson, C. A. G. Rodriguez, Q. Xu, J. Frow, F. Foglia, K. Smith, R. Ravikumar, M. Vinothkannan, N. Mahmoudi, I. Salam, A. P. Periasamy, D. K. Whelligan, M. Mamlouk, H. Lin, B. Seger and J. R. Varcoe, *J. Mater. Chem. A*, 2023, **11**, 20724–20740.
29 D. F. Alves-Lima, X. Li, B. Coulson, E. Nesling, G. A. H. Ludlam, R. Degl'Innocenti, R. Dawson, M. Peruffo and H. Lin, *J. Membr. Sci.*, 2022, **647**, 120329.
30 T. J. Omasta, Y. Zhang, A. M. Park, X. Peng, B. Pivovar, J. R. Varcoe and W. E. Mustain, *J. Electrochem. Soc.*, 2018, **165**, F710.
31 H. Adabi, A. Shakouri, N. U. Hassan, J. R. Varcoe, B. Zulevi, A. Serov, J. R. Regalbuto and W. E. Mustain, *Nat. Energy*, 2021, **6**, 834.
32 X. Zhang, Z. Li, Z. Lu and C. Sun, *J. Chem. Phys.*, 2001, **115**, 10001.
33 J. J. Weeks, *J. Res. Natl. Bur. Stand., Sect. A*, 1963, **67A**, 441.
34 G. R. Strobl, M. J. Schneider and I. G. Voigt-Martin, *J. Polym. Sci., Polym. Phys. Ed.*, 1980, **18**, 1361.
35 W. Rungswang, C. Jarumaneeroj, T. Parawan, P. Jirasukho, S. Juabrum, S. Soontaranon and S. Rugmai, *Polymer*, 2020, **211**, 123096.
36 Y. Jin, A. P. Kotula, C. R. Snyder, A. R. H. Walker, K. B. Migler and Y. J. Lee, *Macromolecules*, 2017, **50**, 6174.
37 J. Rams, A. J. Lopez, M. Sanchez, A. Urena, V. Leal, B. Sanchez-Mariscal and P. Lafuente, *Polym. Test.*, 2012, **31**, 136.
38 J. K. Hobbs, O. E. Farrance and L. Kailas, *Polymer*, 2009, **50**, 4281.
39 F. W. Maine, in *Wood-Polymer Composites*, ed. K. O. Niska and M. Sain, Woodhead publishing, 2008, vol. 10, pp. 208–226.
40 E. Smith and G. Dent, *Modern Raman Spectroscopy*, Wiley, 2nd edn, 2019.
41 T. Motegi, M. Omichi, Y. Maekawa and N. Seko, *Radiat. Phys. Chem.*, 2024, **214**, 111281.
42 R. Espiritu, M. Mamlouk and K. Scott, *Int. J. Hydrogen Energy*, 2016, **41**, 1120.
43 J. J. Frow, A. P. Periasamy, G. Gupta, J. R. Varcoe and H. Lin, *Presented in Part at the 47th International Conference on Infrared and Millimeter Waves*, Netherlands, 2022.
44 A. A. E. Elozeiri, R. G. H. Lammertink, H. H. M. Rijnaarts and J. E. Dykstra, *J. Membr. Sci.*, 2024, **698**, 122538.
45 D. A. Salvatore, C. M. Gabardo, A. Reyes, C. P. O'Brien, S. Holdcroft, P. Pintauro, B. Bahar, M. Hickner, C. Bae, D. Sinton, E. H. Sargent and C. P. Berlinguette, *Nat. Energy*, 2021, **6**, 339.
46 Z. Wang, G. Sun, N. H. C. Lewis, M. Mandal, A. Sharma, M. Kim, J. M. Montes de Oca, K. Wang, A. Taggart, A. B. Martinson, P. A. Kohl, A. Tokmakoff, S. N. Patel, P. F. Nealey and J. J. De Pablo, *Nat. Commun.*, 2025, **16**, 1099.